JACS
JOURNAL OF THE AMERICAN CHEMICAL SOCIETY
Article
Cite This: J. Am. Chem. Soc. XXXX, XXX, XXX−XXX
pubs.acs.org/JACS

Pt-Decorated Composition-Tunable Pd−Fe@Pd/C Core−Shell Nanoparticles with Enhanced Electrocatalytic Activity toward the Oxygen Reduction Reaction

Yin Xiong,[†] Yao Yang,[†] Francis J. DiSalvo, and Héctor D. Abruña*

Department of Chemistry and Chemical Biology, Cornell University, Ithaca, New York 14850, United States

Supporting Information

ABSTRACT: Design of electrocatalysts with both a high-Pt-utilization efficiency and enhanced electrochemical activity is still the key challenge in the development of proton exchange membrane fuel cells. In the present work, Pd−Fe/C bimetallic nanoparticles (NPs) with an optimal Fe composition and decorated with Pt are introduced as promising catalysts toward the oxygen reduction reaction. These bimetallic nanoparticles have a Pd−Fe@Pd core−shell structure with a surface Pt decoration as established through the use of electron energy loss spectroscopy (EELS) and energy-dispersive X-ray (EDX) spectroscopy. These catalysts exhibit excellent electrocatalytic activity ($E_{1/2}$ = 0.866 V vs RHE), increasing the mass activity by more than 70% over that of Pt/C in terms of the total mass of Pt and Pd and by 14 times if only Pt is considered. Simple geometrical calculations, based on spherical core−shell models, indicate that Pd−Fe@Pt has a surface Pt decoration rather than a complete Pt monolayer. Such calculations applied to other examples in the literature point out the need for careful and rigorous arguments about claimed "Pt monolayer/multilayers". Such calculations must be based on not only elemental mapping data but also on the Pt/Pd and other metal atomic ratios in the precursors. Our analysis predicts a minimal Pt/Pd atomic ratio in order to achieve a complete Pt monolayer on the surface of the core materials.

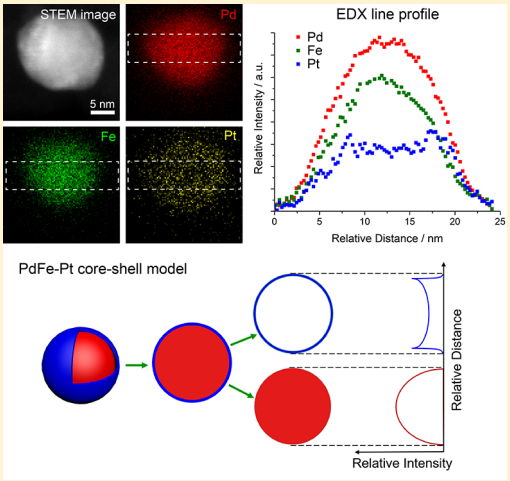

INTRODUCTION

Proton exchange membrane fuel cells (PEMFCs) represent one of the most attractive energy conversion technologies suitable for automotive applications, due to their high power density, high energy conversion efficiency, and potential environmental friendliness.[1−3] However, the large-scale deployment of PEMFCs will require a large amount of Pt for catalysts in order to accelerate the sluggish kinetics of the oxygen reduction reaction (ORR) at the cathode.[4−6] The high cost and scarcity of Pt thus become some of the major hurdles that preclude the broad-based application of PEMFCs (about 35% of the total cost of the fuel cell).

Over the past decades, great efforts have focused on minimizing the Pt loading and increasing its utilization efficiency. A considerable amount of work has been concentrated on developing Pt-based core/Pt-rich shell structures or less expensive core materials with a monolayer of Pt covering the surface.[7−12] A Pt-surface enrichment can be achieved by the thermal treatment in a H_2 gas environment as well as by the selective dealloying of transition-metal-rich PtM bimetallic alloys.[13−17] For example, Wang and co-workers synthesized the intermetallic Pt_3Co with an about two to three atomic-layer Pt shell via annealing at 700 °C, boosting both the mass and specific activity of the catalyst by 10 times.[7] Gan et al. utilized an acid leaching process to activate a Ni-rich Pt alloy, forming Ni-rich core/Pt shell nanoparticles with high electrocatalytic activity.[12] Hu et al. and Wang et al. prepared a class of non-Pt core NPs with a monolayer Pt shell to further boost the electrochemical activity with higher Pt utilization efficiency.[18,19]

However, Pt mono/multilayer coated core−shell catalysts still require a relatively high content of Pt due to the high specific area of nanosized particles. The amount of Pt used in the electrocatalyst can be further lowered by the adoption of electrocatalysts with other metal-based core materials. Pd-based catalysts are attractive alternatives, since Pd possesses promising catalytic properties but has a lower cost than Pt. Many efforts have focused on designing Pd-based nanocrystals, with varying composition, structure, and morphology, such as Pd−Cu alloys with different atomic ratios, Pd−Cu nanocubes, and ultrathin one-dimensional Pd−Ni nanowires.[20−22]Convention: If the strcuture is ordered, we will use chemical formulas as Pd_3Fe. Nevertheless, the incorporation of alloying transition metals with Pd still has a lower electrocatalytic activity than that of Pt/C. Careful design of new materials with desirable structure and surface properties is urgently required for next-generation ORR electrocatalysts.

Received: March 29, 2018
Published: May 21, 2018

DOI: 10.1021/jacs.8b03365
J. Am. Chem. Soc. XXXX, XXX, XXX−XXX

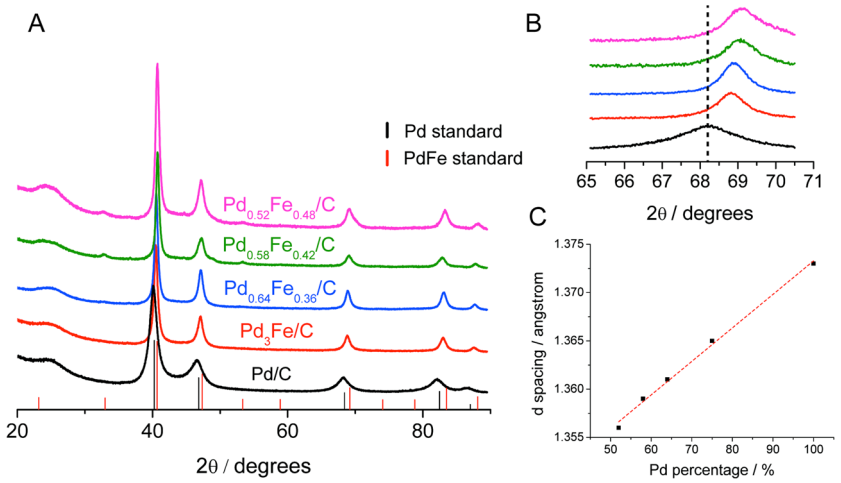

Figure 1. (A) XRD patterns of synthesized Pd–Fe/C bimetallic nanoparticles: Pd/C, Pd_3Fe/C, $Pd_{0.64}Fe_{0.36}$/C, $Pd_{0.58}Fe_{0.42}$/C, and $Pd_{0.52}Fe_{0.48}$/C after annealing at 500 °C for 2 h. The red and black vertical lines correspond to Pd (PDF # 5-681) and PdFe (PDF # 04-003-3875) standard XRD. (B) Graph showing the enlarged region of the Pd(220) diffraction peak. (C) Plot of the *d*-spacing of the (220) peak for Pd–Fe/C with different compositions.

Herein, we report a novel solution-phase synthesis method that provides the flexibility to control the composition of the PdFe bimetallic core with dramatically improved electrocatalytic activity via a minimal Pt decoration of the surface. The incorporation of Fe in the Pd enhances its catalytic activity perhaps due to the lattice strain. Indeed, the electrochemical activity follows a "volcano curve" with increasing amounts of Fe. Moreover, through facile galvanic replacement reactions, a small amount of Pt will decorate the surface of Pd–Fe, and enhance its activity, surpassing that of the state-of-art Pt NPs. Structures of Pd–Fe@Pt/C have been extensively investigated by scanning transmission electron microscopy equipped with electron energy loss spectroscopy and energy-dispersive X-ray spectroscopy. We also show how a simple geometric model can be used to determine the Pt shell thickness from the Pt/Pd atomic ratio.

EXPERIMENTAL SECTION

Chemicals. Palladium acetylacetonate ($Pd(acac)_2$), iron acetylacetonate ($Fe(acac)_3$), triethylene glycol, 1,2-hexadecanediol, sodium hydroxide, potassium tetrachloroplatinate(II) (K_2PtCl_4), and Nafion (5 wt %) were purchased from Sigma-Aldrich. All chemicals were used as received without further purification. Vulcan XC-72 carbon black was from Cabot Corporation.

Synthesis of Pd–Fe@Pd/C and Pt-Decorated Pd–Fe@Pd Nanoparticles. In a typical synthesis, the carbon supported Pd–Fe@Pd/C was prepared in two steps. First, 0.1 mmol of $Pd(acac)_2$ and a predetermined amount of $Fe(acac)_3$ were dissolved in 30 mL of triethylene glycol solution in a three-neck flask. A 120 mg portion of 1,2-hexadecanediol was added to the solution. The solution was then stirred magnetically and ultrasonicated for 15 min with suspended carbon powder (Vulcan-72R) to achieve a 20 wt % metal loading on the carbon support. The well-distributed suspension was purged with Ar for 15 min and heated at 130 °C for 10 min, and then, the temperature was ramped up to 230 °C and kept at 230 °C for 1 h. After cooling down, the mixture was washed with ethanol, acetone, and NaOH/ethanol (1 g of NaOH/10 mL of ethanol) three times, respectively, to remove any remaining surface surfactant.[23] The resulting product was collected by centrifugation and dried at room temperature. The prepared Pd–Fe/C NPs were subsequently annealed under forming gas (95% N_2 and 5% H_2) for 2 h at 500 °C to form Pd–Fe@Pd/C core–shell NPs.[9] Finally, a Pt-decorated Pd–Fe@Pd/C structure was obtained via a galvanic replacement reaction of part of the surface Pd with Pt. Specifically, 20 mg of the Pd–Fe@Pd/C NPs was suspended in 10 mL of 0.04 mM K_2PtCl_4 solution, followed by 30 min of ultrasonication and magnetic stirring at 60 °C for an additional 5 h. The final product was obtained by filtration and dried under room temperature overnight in air. The composition of the Pd–Fe/Pt NPs was determined using ICP-AES (inductively coupled plasma atomic emission spectroscopy), after dissolving the nanoparticles in an aqua regia (HCl + HNO_3) solution. Pt loading of the Pt-decorated Pd–Fe@Pd/C NPs was determined by the difference between the initial mass of K_2PtCl_4 and the residual K_2PtCl_4 in the filtrate after reaction.[19]

Structural Characterization. The crystal structure of all of the synthesized NPs was confirmed by XRD using a Rigaku Ultima IV Diffractometer. Diffraction patterns were collected at a scan rate of 3° min^{-1} at 0.02° steps from 10 to 90°. The metal loading of a series of Pd–Fe/C nanoparticles was found to be 20 wt % using the TGA technique. The weight loss of all Pd–Fe carbon supported catalysts, after being heated to 550 °C, is attributed to both the removal of the carbon support and the oxidation of the Fe elements. Assuming that all Fe formed oxide (Fe_2O_3), the theoretically determined remaining weight should be 22.6, 23.9, 24.8, and 25.7% for Pd_3Fe/C, $Pd_{0.64}Fe_{0.36}$/C, $Pd_{0.58}Fe_{0.42}$/C, and $Pd_{0.52}Fe_{0.48}$/C, respectively, which is very close to the experimental result of 22, 24.5, 25, and 26.7%. STEM images and EELS maps were acquired on a fifth-order aberration-corrected STEM (FEI Titan Themis) operated at 300 keV and with a beam convergence semiangle of 30 mrad. Pd-$M_{4,5}$ and Fe-L_2 edges were used to extract Pd and Fe EELS maps. STEM-EDX elemental maps were acquired using an FEI Tecnai F-20 microscope operated at 200 keV and an Oxford X-Max detector. The beam dose during EDX mapping was about 4 e/(Å^2·s) to achieve more than 10 counts/pixel for the Pt map and more than 70 counts/pixel for the Pd and Fe maps, without a noticeable sample drift. It should be noted that the signal-to-noise (S/N) ratio in EDX map is the square root of X-ray counts/pixel so that S/N of Pd and Fe is larger than 8 and S/N of Pt is larger than 3. Pt-Mα, Pd-Lα, β, and Fe-Kα were used to extract Pt, Pd, and Fe EDX maps, respectively, from the spectrum image.

Electrochemical Characterizations. Electrochemical measurements were performed in 0.1 M $HClO_4$ on a Solartron potentiostat at room temperature. In all electrochemical measurements, 5 mg of the prepared catalyst was mixed with 2 mL of 0.05 wt % Nafion/ethanol solution and subsequently sonicated for approximately 30 min. A 10 μL portion of the resulting catalyst ink was loaded onto the end of a 5 mm diameter glassy carbon electrode, followed by thermal evaporation of the solvent under infrared light. A coiled Pt wire was used as the counter electrode, and Ag/AgCl, in a saturated KCl solution, served as the reference electrode. ORR measurements were carried out on a rotating disk electrode (RDE) in oxygen-saturated 0.1 M $HClO_4$

DOI: 10.1021/jacs.8b03365
J. Am. Chem. Soc. XXXX, XXX, XXX–XXX

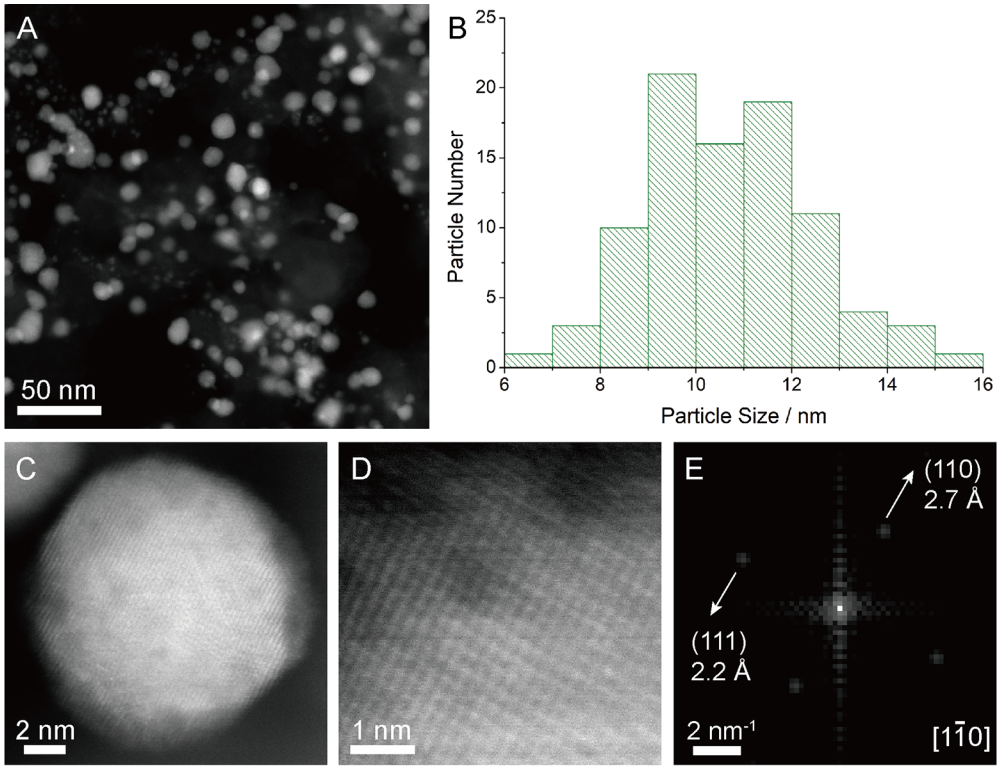

Figure 2. (A, B) HAADF-STEM image of Pd−Fe@Pt nanoparticles and the corresponding histogram of the particle size distribution. (C, D) Atomic-scale STEM image of a particular Pd−Fe@Pt nanoparticle (C) with a magnified region that clearly shows the crystal lattice on the [1−10] zone axis. (E) Fourier transform of lattice images in part D showing the diffraction spots corresponding to the lattice *d*-spacing of the (111) and (110) facets (PDF # 04-003-3875).

solution at a rotation rate of 1600 rpm (bubbling with O_2 for 15 min before scanning and rebubbling for 7 min before the next scan). The ORR profiles were obtained after 50 cycles in 0.1 M $HClO_4$ over the potential range from 0.05 to 1.1 V at 50 mV s^{-1} to remove surface contamination.[24−26] All cyclic voltammetry curves were obtained between 0.05 and 1.1 V at 50 mV/s, and ORR polarization curves were measured at 5 mV/s, from the negative to the positive direction. Durability tests were carried out by continuous scanning cyclic voltammetry from 0.05 to 1 V at 100 mV/s for 4000 cycles. CO stripping experiments were conducted by dosing at 0.05 V vs RHE for 10 min with CO purging and then switched to Ar for another 10 min to remove any remaining CO dissolved in the electrolyte. The scan rate during CO stripping experiments was 50 mV/s over the potential range between 0.05 and 1.2 V.

RESULTS AND DISCUSSION

The Pd−Fe/C bimetallic NPs were prepared via a two-step solution-phase method. First, $Pd(acac)_2$ and $Fe(acac)_3$ were thermally decomposed to form a Pd−Fe alloy in the triethylene glycol solution at 230 °C (details can be found in the Experimental Section). The amount of $Pd(acac)_2$ was fixed to 0.1 mmol, and the amount of $Fe(acac)_3$ was varied from 0.05 to 0.2 mmol, to achieve Pd−Fe/C with various compositions. The as-prepared Pd−Fe/C NPs were annealed at 500 °C for 2 h under forming gas. Due to the high adsorption energy of H on Pd, the surface segregation in an H_2 atmosphere at high temperature leads to the formation of a Pd−Fe@Pd core−shell structure.[18,19] The composition of the synthesized Pd−Fe/C NPs was determined by inductively coupled plasma atomic emission spectroscopy (ICP-AES), and the relative content of Fe in the final products was consistent with the amount of Fe precursor initially added (Figure S1). While the incorporation of transition metals into Pd has been widely reported in previous studies to facilitate the ORR kinetics,[7,13−17] we later discovered that the activity could be further enhanced by minimal surface decoration with Pt. The process can be simply achieved through a galvanic replacement reaction of Pd with Pt in a very dilute $PtCl_4^{2-}$ solution (detailed information in the Experimental Section).

The XRD patterns of postannealed Pd−Fe/C NPs and control Pd/C are shown in Figure 1. The broad peak at around 25° is ascribed to the carbon support. The remaining peaks, from left to right, correspond to the (111), (200), (220), (311), and (222) planes, respectively, in a face-centered cubic (fcc) alloy structure. The XRD patterns also showed small (110) at 33° and (210) at 53° ordering peaks in Pd−Fe/C, which are consistent with the standard database (PDF # 04-003-3875). Figure 1B clearly shows that, with a higher fraction of Fe in Pd−Fe/C alloy NPs, the diffraction peaks shift to higher angles, which is due to the smaller size of Fe relative to Pd. Figure 1C shows the dependence of Pd composition on the *d* spacing, which indicates the linear relationship between them. The domain size was calculated to be about 10 nm from the (220) peak width via the Scherrer equation, with detailed information listed in Table S1. This is similar to the particle size observed in TEM images. Since the domain size and the particle size are similar, the nanoparticles are single crystals, not polycrystalline aggregates.

Single-phase Pd−Fe NPs with a uniform size distribution are suitable for Pt surface decoration. Figure S2 compares the morphology and particle size of Pd−Fe/C and Pt-decorated Pd−Fe/C, from low-magnification TEM images. Both of them exhibited an average particle size of about 10 nm and a uniform distribution on the carbon support, with no discernible

DOI: 10.1021/jacs.8b03365
J. Am. Chem. Soc. XXXX, XXX, XXX−XXX

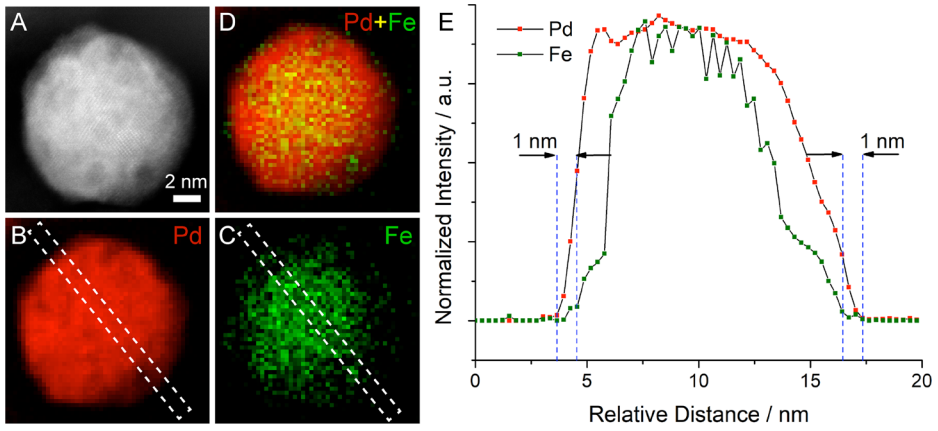

Figure 3. (A) STEM image of Pd−Fe@Pt. (B−D) EELS elemental maps of Pd (red) and Fe (green) and composite map of Pd vs Fe (D). (E) EELS elemental line profiles of Pd and Fe extracted from white dashed boxes from the EELS mapping in parts B and C, respectively.

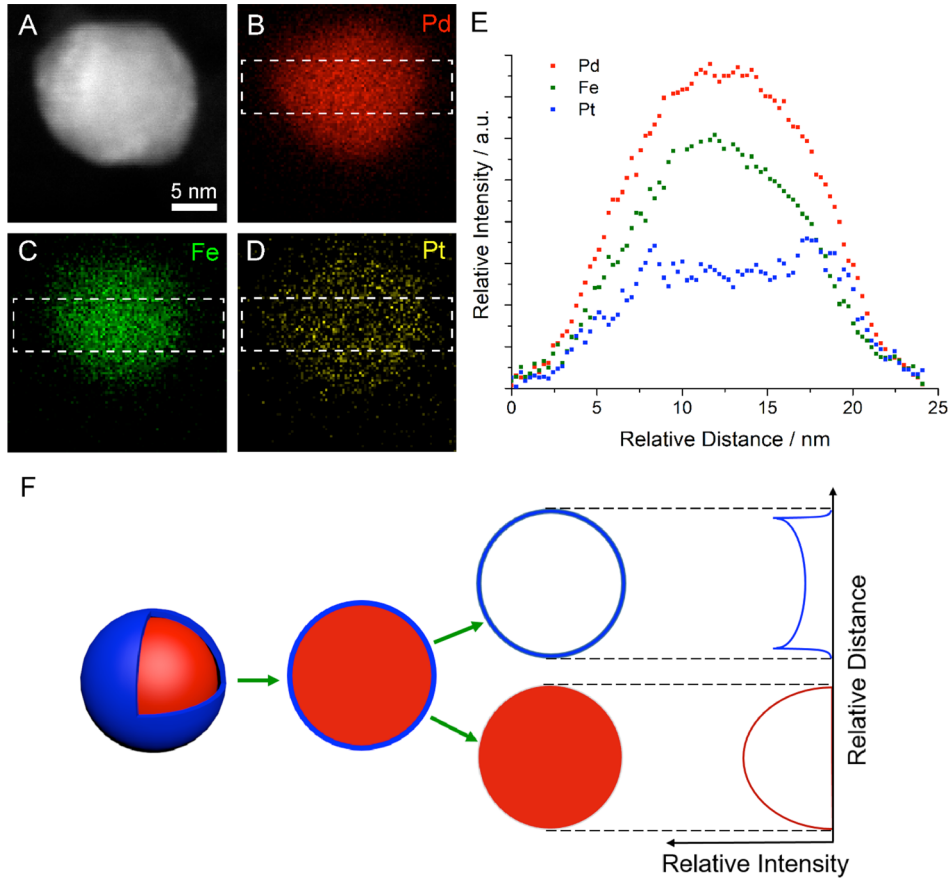

Figure 4. (A) STEM image of a PdFe@Pt nanoparticle. (B−D) EDX elemental maps of Pd (red), Fe (green), and Pt (yellow). (E) EDX line profiles of Pd (red), Fe (green), and Pt (blue) extracted from white dashed boxes from the EDX mapping in parts B−D. (F) Schematic model of a core−shell spherical particle and the theoretical projected intensity profiles.

differences in morphology. The spontaneous, yet mild, replacement reaction provides a controllable approach for surface decoration without causing damage to the structure. Here, we decorated the Pd−Fe/C bimetallic NPs with a composition of $Pd_{0.58}Fe_{0.42}/C$ due to their optimal electrochemical properties, which will be discussed in detail later (vide infra).

The crystallographic and chemical information on Pt-decorated $Pd_{0.58}Fe_{0.42}/C$ (simplified as PdFe@Pt/C in the following discussions) has been further explored using an aberration-corrected scanning transmission electron microscope (STEM) equipped with an electron energy loss spectrometer (EELS) operated at 300 keV. STEM images in Figure 2A,B show PdFe@Pt/C nanoparticles with a narrow size distribution and an average particle size of around 10 nm in diameter, which is consistent with the grain size calculated from XRD. In Figure 2C−E, the atomic-scale STEM image of a single particle and the corresponding Fourier transform reveal the lattice *d*-space of the (111) (2.2 Å) and (110) (2.7 Å) planes projected on the [1−10] zone axis, which match the

DOI: 10.1021/jacs.8b03365
J. Am. Chem. Soc. XXXX, XXX, XXX−XXX

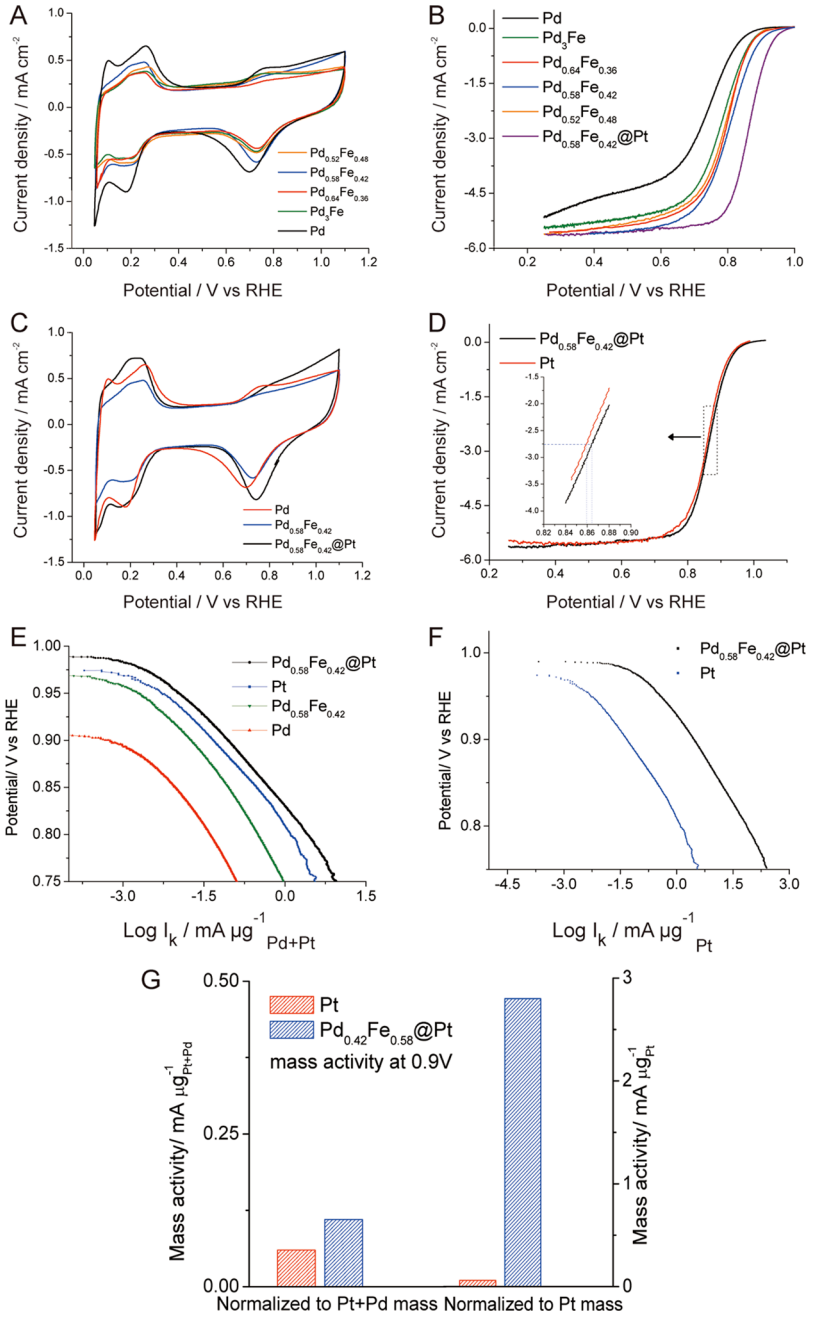

Figure 5. Electrocatalytic properties of synthesized Pd–Fe/C and Pd–Fe@Pt/C nanoparticles. (A) Cyclic voltammetry (CV) profiles of synthesized Pd–Fe/C NPs in Ar-saturated 0.1 M $HClO_4$ solution, scanned at a rate of 50 mV/s at room temperature. (B) ORR polarization curves in O_2-saturated 0.1 M $HClO_4$ at a scan rate of 5 mV/s and a rotation rate of 1600 rpm. (C) CV profiles of Pd/C, $Pd_{0.58}Fe_{0.42}$/C, and $Pd_{0.58}Fe_{0.42}$@Pt/C in Ar-purged 0.1 M $HClO_4$ solution at a sweep rate of 50 mV/s. (D) Comparison of ORR polarization curves for Pt/C and $Pd_{0.58}Fe_{0.42}$@Pt/C in O_2-saturated 0.1 M $HClO_4$ solution at a scan rate of 5 mV/s and a 1600 rpm rotation rate. (E) Tafel plots. Mass activities of different catalysts, normalized to the total mass of Pd and Pt. (F) Tafel plots. Mass activity of Pt/C and $Pd_{0.58}Fe_{0.42}$@Pt/C, normalized to the mass of Pt. (G) Comparison of the mass activity between Pt/C and $Pd_{0.58}Fe_{0.42}$@Pt/C, at 0.9 V vs RHE.

(111) (2.22 Å) and (110) (2.71 Å) in the standard PdFe XRD (PDF # 04-003-3875). The (110) plane is recognized as the characteristic diffraction feature of ordered intermetallics, which is consistent with the (110) intermetallic peak at 33° in the XRD profile in the Figure 1.[7] The chemical composition information was obtained using EELS elemental mapping in the STEM model. Parts B–D of Figure 3 show the Pd (red), Fe (green), and their composite maps, extracted from the Pd-$M_{4,5}$ edge and the Fe-L_2 edge in the EELS spectra (Figure S3). The presence of a thin Pd shell can be clearly distinguished from the thin red region in the Pd vs Fe composite map. The precise thickness of the Pd shell was quantitatively analyzed by extracting EELS line profiles from the Pd and Fe maps. Figure 3E indicates a Pd shell thickness of about 1 nm, which corresponds to a three-atomic-layer-thick Pd shell on the surface. The thin Pd shell could serve as a protection layer to prevent the dissolution of Fe in the acid media during the electrochemical cycling while being thin enough to maintain the superior ORR electrocatalytic activity of the PdFe intermetallic core.

DOI: 10.1021/jacs.8b03365
J. Am. Chem. Soc. XXXX, XXX, XXX–XXX

Because of the low Pt content in PdFe@Pt (Pt:Pd = 1:70), the EELS signal-to-noise ratio of Pt-$M_{4,5}$ edges was not high enough to get a reliable Pt map. Instead, energy-dispersive X-ray (EDX) spectroscopy served as a reliable tool to detect the trace amount of Pt on the nanoparticles.

To demonstrate the presence of surface decoration, we employed EDX spectroscopy in STEM mode to study the elemental distribution of Pt vs Pd and Fe in Pd−Fe@Pt. The EDX spectrum in Figure S4 shows a strong Pt-Mα edge, which, together with the Pd-Lα, β, and Fe-Kα edges, can be used for EDX elemental mapping. Parts A−D of Figure 4 present the STEM image of a typical Pd−Fe@Pt nanoparticle and the corresponding EDX elemental maps of Pd (red), Fe (green), and Pt (yellow). In order to quantitatively study the elemental distribution, we extracted EDX elemental line profiles (Figure 4E) from the corresponding elemental maps (white dashed boxes in Figure 4B−D). Pd and Fe exhibit bell-shaped line profiles, whereas Pt shows a plateau with two distinguishable edges. The schematic in Figure 4F illustrates the theoretical projected intensity profile of core−shell particles, indicating that Pd and Fe will ideally present a semicircular intensity profile while the surface Pt layer will exhibit a slightly lower intensity in the middle with two noticeable sharp edges. The differences between the experimental data and the schematic are likely due to the blurring effects from the larger electron beam size employed in EDX mapping. That means the experimental EDX line profiles can be rationalized as the combined result of the intensity profile in the schematic and a Gaussian blurring (smoothing) function. However, the key features of the EDX line profiles and the schematic are quite similar and indicate that Pt decorates the surface of the Pd−Fe@Pd core−shell nanoparticles. The presence of a small amount of Pt decoration was also verified by XPS results, as shown in Figure S5.

The cyclic voltammetric profiles (CVs) of the Pd−Fe/C bimetallic NPs, with different Fe contents were obtained in an Ar-saturated 0.1 M $HClO_4$ solution at a scan rate of 50 mV/s, and all are shown in Figure 5A. These distinct hydrogen regions show the incorporation of Fe partially alters the electronic properties of Pd, and modifies the adsorption of hydrogen. Compared to Pd/C, the cathodic peak (around 0.7 V) of the Pd−Fe/C bimetallic catalysts exhibits a positive shift, which indicates a decreased adsorption free energy for the oxygen-containing species and a faster rate of reduction of the Pd surface oxide.[27−29] To better understand the relationship between lattice strain and electrochemical activity, the catalytic performance toward the ORR of different catalysts was characterized by rotating disk electrode (RDE) in O_2-saturated 0.1 M $HClO_4$ solution at 1600 rpm. The polarization curves are profiled in Figure 5B. The diffusion limited current of about −5.5 mA/cm^2 at 1600 rpm indicates that all of the Pd−Fe/C bimetallic NPs are effective in the four-electron transfer reduction process.[30,31] Compared to Pd/C, Pd−Fe/C bimetallic NPs exhibit a positive shift in the onset potential, indicating that alloying of Pd with Fe enhances the ORR kinetics and lowers the overpotential. The half-wave potentials ($E_{1/2}$) of the Pd−Fe/C NPs are also positively shifted, to a different extent, depending on composition, following the order: Pd/C < Pd_3Fe/C < $Pd_{0.52}Fe_{0.48}$/C < $Pd_{0.64}Fe_{0.36}$/C < $Pd_{0.58}Fe_{0.42}$/C. The electrocatalytic performance of the series of Pd−Fe/C NPs shows a "volcano trend" with increasing Fe content, which could be explained via Norskov's d-band center theory.[32,33] The surface electronic structure of the NPs will be affected by two main aspects: the lattice constant (strain) and the ligand effect. Initially, as the Fe content increases, the lattice constant contraction (strain) dominates. This weakens the adsorption energy of the oxygen-containing intermediate species and thus enhances the electrocatalytic activity. Subsequently, with further increases in the amount of Fe, the ligand effect becomes more pronounced and plays a more important role, lowering the electrochemical activity. Overall, those two opposite influences might contribute to the "volcano trend" in the electrocatalytic performance.

Taking this into account, $Pd_{0.58}Fe_{0.42}$/C NPs with the highest ORR activity were decorated with Pt in an effort to further enhance its ORR activity. Pt decoration, or monolayer surface covering, has been extensively recognized as an effective approach to promote ORR kinetics with low Pt loading. The CVs of Pd/C and $Pd_{0.58}Fe_{0.42}$/C before and after Pt decoration are shown in Figure 5C. The cathodic peak of $Pd_{0.58}Fe_{0.42}$/C exhibits a positive shift when compared to Pd/C and shifts further positive after Pt decoration, demonstrating faster hydroxyl adsorption/desorption after the incorporation of Fe and surface Pt decoration. The polarization profiles of Pt-decorated $Pd_{0.58}Fe_{0.42}$/C and Pt/C are profiled in Figure 5D. The half-wave potential of Pt-decorated $Pd_{0.58}Fe_{0.42}$/C surpassed that of Pt/C by 7 mV. To quantitatively evaluate the electrochemical activity, the kinetic currents of $Pd_{0.58}Fe_{0.42}$@Pt/C and Pt/C were calculated using the Koutecky−Levich equation,[34] normalized to the total mass of Pt and Pd (Figure 5E) and Pt (Figure 5F), respectively. The mass activity of the Pt-decorated $Pd_{0.58}Fe_{0.42}$/C, normalized to all noble metals (Pt + Pd), increased by 70% when compared with Pt, and exhibited a 14-fold enhancement when normalized to Pt only (Figure 5G). The enhancement could be attributed to the combination effect of strain, arising from the lattice mismatch, and electronic modification.

CO-stripping was used to further characterize surface electronic properties of the Pt-decorated Pd−Fe NP, as is shown in Figure S6. The the CO-oxidation peak potential of Pt-decorated $Pd_{0.58}Fe_{0.42}$/C (0.941 V) was between that of Pd/C (0.959 V) and Pt/C (0.918 V), with a positive shift compared to Pd/C, indicating Pt and Pd can coexist on the surface of the electrocatalysts with a weakening of the CO adsorption energy related to Pd/C. Durability tests were also conducted for Pt-decorated $Pd_{0.58}Fe_{0.42}$/C in Ar-saturated 0.1 M $HClO_4$ solution for 4000 cycles between 0.05 and 1 V vs RHE. The CV and ORR polarization curves, before and after testing, are shown in Figure S7. While there is a 25 mV negative shift in the half-wave potential, we believe it is due, at least in part, to the loss of electrochemical surface area (ECSA) due to particle aggregation/coalescence after extensive potential cycling. STEM imaging and EDX spectroscopy were employed to investigate the structural and chemical evolution after cycling. As shown in Figure S8, STEM images of five different regions of Pd−Fe@Pt after electrochemical cycles and particle aggregation/coalescence can be clearly observed, indicated by the dashed boxes in parts B−E. The overall particle size distribution (PSD) was analyzed for around 400 particles in images A−E. It exhibits a broader size distribution and larger average particle size (about 20 nm) when compared to the PSD of as-synthesized Pd−Fe@Pt in Figure 2B. STEM-EDX was used to quantitatively analyze the relative amount of Pd, Fe, and Pt before and after electrochemical cycles. The relative amounts of Fe, Pd, and Pt were calculated from the EDX spectra (Figure S9) and shown in Table S2. After electrochemical cycles, the relative amount of

DOI: 10.1021/jacs.8b03365
J. Am. Chem. Soc. XXXX, XXX, XXX−XXX

Fe dropped by about 50%, indicating a significant loss of Fe due to the Fe dissolution in acid electrolyte. Given the statistical errors in EDX measurements, the Pt/Pd ratio remained relatively constant, suggesting no significant Pt dissolution.

On the basis of the EDX elemental mapping results that indicated Pt surface decoration of the PdFe NPs and the coexistence of Pt and Pd on the surface, from CO stripping, we further investigated what is the effective friction of the Pt layer on this core−shell catalyst from a theoretical perspective. Assuming that Pd−Fe@Pt is a spherical particle, with a diameter of D and a shell thickness of x, the theoretical Pd to Pt atomic ratio (Pd/Pt) will be a function of x, as described in the equation in Figure 6. The relation between Pd/Pt and shell

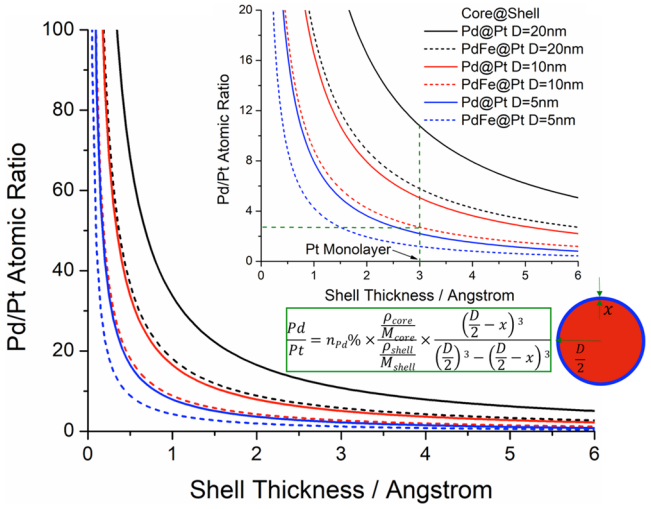

Figure 6. Theoretical calculations of the Pd/Pt atomic ratio as a function of the particle size (diameter, D) and the shell thickness (x). The inset shows the magnified diagram with a focus on lower Pd/Pt atomic ratio, i.e., higher relative Pt content. Solid lines are Pd@Pt core−shell particles, while dashed lines are PdFe@Pt. The crossing point of the two dashed green lines is for PdFe@Pt with D = 10 nm, which has to have a Pt/Pd ratio larger than 1:2.7 to achieve a complete Pt monolayer (3 Å). n_{Pd}% in the equation is the mole fraction of Pd in the core materials (e.g., n_{Pd}% = 0.5 in PdFe). Details of the equation derivation can be found in the Supporting Information.

thickness was systematically studied for both pure Pd cores (solid lines) and bimetallic PdFe cores (dashed lines) with a series of particles of different size (Figure 6). The Pd/Pt atomic ratio decays dramatically, as the shell thickness increases, for all different particle sizes, indicating that much more Pt is required for a thicker Pt shell, and thus, the average cost of such a core−shell catalyst will increase significantly. Furthermore, the Pd/Pt atomic ratio also decreases for a constant thickness while the particle size changes from 20 to 5 nm, which indicates that smaller particles will have a larger Pt mole fraction and, thus, a higher average cost of precious metals. For the same particle size, Pd−Fe@Pt exhibits a Pd/Pt atomic ratio only about half as large as Pd@Pt because the Pd mole fraction in the Pd−Fe core is only 50% of that of a pure Pd core. In summary, overall precious metal loading could be minimized (optimized) if one could design a core−shell catalyst with a thin shell (ideally monolayer), a core with a smaller Pd mole fraction, and a relatively larger particle size. It is worth noting that these design principles also need to accommodate the consideration of the effective electrochemical surface area per mass of the core−shell catalyst and the increasing cost of core materials in a larger particle size.

In the case of a 10 nm Pd−Fe@Pt particle (red dashed line), the Pt/Pd atomic ratio has to be larger than 1:2.7 and thus the Pt mole fraction has to be more than a quarter in total precious metal loading, to achieve a Pt monolayer with 100% coverage. If Pt/Pd ratios can be determined from experiments, such as ICP-AES, one could work out the actual shell thickness on the basis of the experimental Pt/Pd atomic ratio and compare it with EELS or EDX elemental mapping results. Surprisingly, in this work, the Pt/Pd ratio was determined to be about 1:70 (much smaller than 1:2.7 for a complete Pt monolayer) on the basis of ICP-AES, which would predict a shell thickness far less than a Pt monolayer (about 3 Å). The term "Pt surface decoration" rather than "Pt monolayer" was thus used in this work to more rigorously and precisely describe Pd−Fe@Pt. Despite numerous claims in the literature of core−shell structures with "Pt monolayer/multilayers", on the basis of their EELS or EDX elemental mapping or line profiles (Table S3), the measured Pt content was, in fact, insufficient for a fully covered Pt layer and can be readily calculated from this spherical core−shell model.[7,9,19,35−39] Therefore, both core and shell materials are clearly on the surface and can participate in electrocatalysis in many known core−shell electrocatalysts. We believe that the "back-of-the-envelope" calculations presented in this work should always be considered before synthesizing core−shell electrocatalysts. The diagram and simple equation developed in Figure 6 can be used as a guide to work out the minimal Pt/M ratio in the precursors required to form a complete Pt monolayer or multilayers in the design of M@Pt core−shell electrocatalysts.

CONCLUSION

In summary, the Pt-decorated $Pd_{0.58}Fe_{0.42}$/C NPs with tunable core composition and surface Pt decoration have been synthesized via a method involving thermal decomposition, H_2-induced surface segregation, and galvanic replacement reaction. The optimal Pd−Fe/C bimetallic nanoparticles exhibited excellent electrochemical performance toward ORR after surface decoration with ultralow amounts of Pt (around 1 at. %). In addition, since non-Pt NPs with Pt surface decoration and monolayer coating are promising and popular candidates for ORR catalysts, we have also discussed the minimal Pt/Pd required for a monolayer coverage of Pt. For fuel cell catalysts, at the scale of 5−20 nm, a relatively high amount of Pt content is required even for a Pt monolayer. Compared with a full Pt monolayer coating, the use of Pt surface decoration enables an ultralow Pt loading while retaining the high activity of the Pd−Fe@Pd core−shell catalysts. The electrocatalyst also maintained a moderate durability during electrochemical cycles. The experimental design and theoretical calculations described in this work provide a novel approach to design higher-efficiency and lower-cost electrocatalysts for the oxygen reduction reaction.

ASSOCIATED CONTENT

Supporting Information

The Supporting Information is available free of charge on the ACS Publications website at DOI: 10.1021/jacs.8b03365.

Structural, chemical, and electrochemical characterization of PdFe@Pt nanoparticles in Figures S1−S9 and Tables S1−S3 (PDF)

DOI: 10.1021/jacs.8b03365
J. Am. Chem. Soc. XXXX, XXX, XXX−XXX

AUTHOR INFORMATION

Corresponding Author

*hda1@cornell.edu

ORCID

Yao Yang: 0000-0003-0321-3792

Héctor D. Abruña: 0000-0002-3948-356X

Author Contributions

†Y.X. and Y.Y. contributed equally to this work.

Notes

The authors declare no competing financial interest.

ACKNOWLEDGMENTS

This work made use of TEM and XPS facilities of the Cornell Center for Materials Research (CCMR) which are supported through the National Science Foundation Materials Research Science and Engineering Center (NSF MRSEC) program (DMR-1719875). We appreciate the inspired discussion about the schematic model for EDX mapping with Elliot Padgett in Prof. David Muller's group in School of Applied & Engineering Physics at Cornell as well as Gary Chen in Prof. Bruce van Dover's group for the help with XPS. We thank Rui Zeng at Cornell for editing the manuscript.

REFERENCES

(1) Gasteiger, H.; Markovic, N. M. *Science* **2009**, *324*, 48.
(2) Debe, M. *Nature* **2012**, *486*, 43.
(3) Arico, A. S.; Bruce, P.; Scrosati, B.; Tarascon, J. M.; Van Schalkwijk, W. *Nat. Mater.* **2005**, *4*, 366.
(4) Wang, J.; Zhao, N.; Fang, B.; Li, H.; Bi, X. T.; Wang, H. *Chem. Rev.* **2015**, *115*, 3433.
(5) Guo, S.; Zhang, S.; Sun, S. *Angew. Chem., Int. Ed.* **2013**, *52*, 8526.
(6) Zhao, X.; Chen, S.; Fang, Z.; Ding, J.; Sang, W.; Wang, Y.; Zhao, J.; Peng, Z.; Zeng, J. *J. Am. Chem. Soc.* **2015**, *137*, 2804.
(7) Wang, D.; Xin, H. L.; Hovden, R.; Wang, H.; Yu, Y.; Muller, D. A.; DiSalvo, F. J.; Abruña, H. D. *Nat. Mater.* **2013**, *12*, 81.
(8) Strasser, P.; Koh, S.; Anniyev, T.; Greeley, J.; More, K.; Yu, C. F.; Liu, Z. C.; Kaya, S.; Nordlund, D.; Ogasawara, H.; Toney, M. F.; Nilsson, A. *Nat. Chem.* **2010**, *2*, 454.
(9) Wang, D.; Xin, H. L.; Yu, Y.; Wang, H.; Rus, E.; Muller, D. A.; Abruña, H. D. *J. Am. Chem. Soc.* **2010**, *132*, 17664.
(10) Oezaslan, M.; Heggen, M.; Strasser, P. *J. Am. Chem. Soc.* **2012**, *134*, 514.
(11) Wu, Y.; Wang, D.; Niu, Z.; Chen, P.; Zhou, G.; Li, Y. *Angew. Chem., Int. Ed.* **2012**, *51*, 12524.
(12) Gan, L.; Heggen, M.; Rudi, S.; Strasser, P. *Nano Lett.* **2012**, *12*, 5423.
(13) Ruban, A. V.; Skriver, H. L.; Nørskov, J. K. *Phys. Rev. B: Condens. Matter Mater. Phys.* **1999**, *59*, 15990.
(14) Wang, L.-L.; Johnson, D. D. *J. Am. Chem. Soc.* **2009**, *131*, 14023.
(15) Dubau, L.; Maillard, F.; Chatenet, M.; André, J.; Rossinot, E. *Electrochim. Acta* **2010**, *56*, 776.
(16) Chen, S.; Gasteiger, H. A.; Hayakawa, K.; Tada, T.; Shao-Horn, Y. J. *J. Electrochem. Soc.* **2010**, *157*, A82.
(17) Cui, C.; Gan, L.; Heggen, M.; Rudi, S.; Strasser, P. *Nat. Mater.* **2013**, *12*, 765.
(18) Hu, J.; Wu, L.; Kuttiyiel, K.; Goodman, K.; Zhang, C.; Zhu, Y.; Vukmirovic, M.; White, M.; Sasaki, K.; Adzic, R. *J. Am. Chem. Soc.* **2016**, *138*, 9294.
(19) Wang, G.; Huang, B.; Xiao, L.; Ren, Z.; Chen, H.; Wang, D.; Abruña, H.; Lu, J.; Zhuang, L. *J. Am. Chem. Soc.* **2014**, *136*, 9643.
(20) Zheng, Y.; Zhao, S.; Liu, S.; Yin, H.; Chen, Y.; Bao, J.; Han, M.; Dai, Z. *ACS Appl. Mater. Interfaces* **2015**, *7*, 5347.
(21) Gao, Q.; Ju, Y.; An, D.; Gao, M.; Cui, C.; Liu, J.; Cong, H.; Yu, S. *ChemSusChem* **2013**, *6*, 1878.
(22) Liu, H.; Koenigsmann, C.; Adzic, R.; Wong, S. *ACS Catal.* **2014**, *4*, 2544.
(23) Arán-Ais, R.; Vidal-Iglesias, F.; Solla-Gullón, J.; Herrero, E.; Feliu, J. *Electroanalysis* **2015**, *27*, 945.
(24) Arico, A. S.; Stassi, A.; Modica, E.; Ornelas, R.; Gatto, I.; Passalacqua, E.; Antonucci, V. *J. Power Sources* **2008**, *178*, 525.
(25) Stamenkovic, V.; Schmidt, T. J.; Ross, P. N.; Markovic, N. M. *J. Phys. Chem. B* **2002**, *106*, 11970.
(26) Gasteiger, H. A.; Kocha, S. S.; Sompalli, B.; Wagner, F. T. *Appl. Catal., B* **2005**, *56*, 9.
(27) Zhao, X.; Chen, S.; Fang, Z.; Ding, J.; Sang, W.; Wang, Y.; Zhao, J.; Peng, Z.; Zeng, J. *J. Am. Chem. Soc.* **2015**, *137*, 2804.
(28) Hu, J.; Kuttiyiel, K.; Sasaki, K.; Su, D.; Yang, T.-H.; Park, G.-G.; Zhang, C.; Chen, G.; Adzic, R. R. *Catalysts* **2015**, *5*, 1321.
(29) Van der Vliet, D. F.; Wang, C.; Li, D.; Paulikas, A. P.; Greeley, J.; Rankin, R. B.; Strmcnik, D.; Tripkovic, D.; Markovic, N. M.; Stamenkovic, V. R. *Angew. Chem., Int. Ed.* **2012**, *51*, 3139.
(30) Wang, C.; Daimon, H.; Onodera, T.; Koda, T.; Sun, S. *Angew. Chem., Int. Ed.* **2008**, *47*, 3588.
(31) Niu, W.; Li, L.; Liu, X.; Wang, N.; Liu, J.; Zhou, W.; Tang, Z.; Chen, S. *J. Am. Chem. Soc.* **2015**, *137*, 5555.
(32) Mavrikakis, M.; Hammer, B.; Norskov, J. K. *Phys. Rev. Lett.* **1998**, *81*, 2819.
(33) Hammer, B.; Hansen, L. B.; Norskov, J. K. *Phys. Rev. B: Condens. Matter Mater. Phys.* **1999**, *59*, 7413.
(34) Bard, A. J.; Faulkner, L. R. *Electrochemical Methods: Fundamentals and Applications*; Wiley: New York, 2001; p 341.
(35) Shao, M.; Shoemaker, M.; Peles, A.; Kaneko, K.; Protsailo, L. *J. Am. Chem. Soc.* **2010**, *132*, 9253.
(36) Zhang, Y.; Hsieh, Y.-C.; Volkov, V.; Su, D.; An, W.; Si, R.; Zhu, Y.; Liu, P.; Wang, J. X.; Adzic, R. R. *ACS Catal.* **2014**, *4*, 738.
(37) Kongkanand, A.; Subramanian, N.; Yu, Y.; Liu, Z.; Igarashi, H.; Muller, D. A. *ACS Catal.* **2016**, *6*, 1578.
(38) Wang, X.; Vara, M.; Luo, M.; Huang, H.; Ruditskiy, A.; Park, J.; Bao, S.; Liu, J.; Howe, J.; Chi, M.; Xie, Z.; Xia, Y. *J. Am. Chem. Soc.* **2015**, *137*, 15036.
(39) Hu, J.; Wu, L.; Kuttiyiel, K.; Goodman, K. R.; Zhang, C.; Zhu, Y.; Vukmirovic, M. B.; White, M. G.; Sasaki, K.; Adzic, R. R. *J. Am. Chem. Soc.* **2016**, *138*, 9294.

DOI: 10.1021/jacs.8b03365
J. Am. Chem. Soc. XXXX, XXX, XXX−XXX